Journal of Applied Geophysics 101 (2014) 42–50

Contents lists available at ScienceDirect

Journal of Applied Geophysics

journal homepage: www.elsevier.com/locate/jappgeo

Integrating EMI and GPR data to enhance the three-dimensional reconstruction of a circular ditch system

Timothy Saey [a,*], Samuël Delefortrie [a], Lieven Verdonck [b], Philippe De Smedt [a], Marc Van Meirvenne [a]

[a] Department of Soil Management, Ghent University, Coupure Links 653, 9000 Gent, Belgium
[b] Department of Archaeology, Ghent University, Sint-Pietersnieuwstraat 35, 9000 Gent, Belgium

ARTICLE INFO

Article history:
Received 2 July 2013
Accepted 8 November 2013
Available online 20 November 2013

Keywords:
Ground-penetrating radar
Depth slices
Electromagnetic induction
Inversion
Wave velocities

ABSTRACT

Ground Penetrating Radar (GPR) reflections occur at sharp interfaces between contrasting soil layers. Generally, the depth of the interface is expressed as the two-way travel time from the transmitting to the receiving antenna. Converting these travel times to depths requires knowledge of the propagation speed of the GPR wave in the soil. This velocity is influenced by the electric properties of the soil water content, mainly by the dielectric permittivity (ε). The soil electrical conductivity (σ), which also depends on the soil water content, can be accounted for by electromagnetic (EMI) induction prospecting. A procedure was proposed to thoroughly characterize a circular ditch system by inverting the apparent electrical conductivity (σ_a) measurements from a multi-receiver EMI instrument based on GPR profile data. A fitting procedure allowed to calibrate both the propagation speed of the GPR waves up to the interface between the ditch infilling and the underlying sand and the conductivities of both layers. Integrating the simultaneous EMI measurements and high-resolution GPR depth profiles and – slices improved the non-invasive dimensioning of the circular ditch system.

1. Introduction

A combination of geophysical surveying techniques holds considerable promise to map a wide range of soil features (Kvamme, 2006). Ground-penetrating radar (GPR) and electromagnetic induction (EMI) employed in mobile arrays are effective geophysical techniques for fast, high-resolution and non-invasive determination of shallow subsurface properties through the measurement of soil electrical properties (Jol, 2009; Reynolds, 1997).

The GPR wave propagation is mainly correlated to the depth-dependent dielectric permittivity (ε) while EMI field propagation is mainly sensitive to the soil electrical conductivity (σ), which are in a non-saline soil essentially affected by both soil texture and soil water content (Huisman et al., 2003; Saey et al., 2009b). GPR reflection data can be used to map the sedimentary structure of the subsurface in great detail (Lunt et al., 2005), because the high-frequency electromagnetic waves are reflected at interface boundaries. Contrary, multi-receiver EMI instruments allow integrating the σ_a of overlapping soil volumes to map the soil stratigraphy (Beamish, 2011), because the different coil configurations provide simultaneous measurements with different depth sensitivity. Saey et al. (2009a, 2012) modeled the interface depths between contrasting soil layers in a two- and three-layered soil. Compared with EMI, GPR provides a higher resolution of subsurface features. GPR is able to display discrete texture or reflection patterns in its profiles, because the waves reflect very distinctly on the boundaries between different layers. It measures the time it takes to travel from an antenna to such an interface and back (two-way travel time t), called a time-distance record of the subsurface. In order to convert these times into absolute depths (z), the velocity of the wave propagation (v) must be known. However, this v needs to be determined for each particular soil textural composition at different moisture conditions. Therefore, this v should be considered with respect to σ, as a perfect integrator of the bulk soil textural composition and moisture status. Moreover, σ of the soil affects the attenuation of the high-frequency electromagnetic waves (Sucre et al., 2011). Integrating GPR profiles with the surface-covered EMI measurements shows potential to enable an accurate determination of this v, while EMI inversion could be calibrated with the high-resolution GPR time-record.

We propose to combine both structural information derived from both GPR and EMI data to accurately model the interface depth in a two-layered soil. Therefore, we aim at investigating the extent to which GPR-derived interfaces can improve the inversion of multi-receiver EMI measurements and inversely, how EMI can help in determining the v of GPR waves in a particular soil. The integrated methodology will be evaluated on its potential to allow the three-dimensional characterization of a circular ditch system.

2. Materials and methods

2.1. Study site

Our study site is situated in the north of Belgium (Fig. 1). The study site is situated in the Flemish Valley. The geological substrate of this

* Corresponding author. Tel.: +32 9 264 60 42; fax: +32 9 264 62 47.
E-mail address: Timothy.Saey@UGent.be (T. Saey).

0926-9851/$ – see front matter © 2013 Elsevier B.V. All rights reserved.
http://dx.doi.org/10.1016/j.jappgeo.2013.11.004

Fig. 1. Localization of the study site in Belgium (red boundary) and delineation on the aerial photograph of 1996. (For interpretation of the references to color in this figure legend, the reader is referred to the web version of this article.)

landscape is composed of marine deposits from Eocene and Oligocene origin. A 20–30 m deep valley has been eroded during the Lower and Middle Pleistocene Quaternary periods. During the Eamian glacial stage, this valley was mainly filled up with niveo-fluviatile loamy material and niveo-eolic cover sands. The topography of the Flemish Valley can be considered flat, with a little pronounced microrelief (Sys and Vandenhoudt, 1974). Across the pasture field containing the study site, a few soil samples were taken from the sand and the clay substrate and analyzed for their textural composition according to the conventional sieve–pipette method. The mean clay–silt–sand fractions (with boundaries 2–50–2000 μm, respectively) were determined. On average, the topsoil has a large sand content (79.0%) and a very low clay content (4.5%).

On the national soil map (scale 1:20 000) two dominant soil series (Zdp and Zcc) are indicated for the site. These symbols represent: a sandy topsoil texture (Z), moderately wet conditions (d) or slightly wet conditions (c) without profile development (p) or with a strongly spotted texture B-horizon (c).

On this site, two concentric circular ditches were found as cropmarks by aerial photography in 1996. An area of 0.75 ha was selected on the pasture field containing the ditches (central coordinates 51°13′06″N and 3°45′55″E). The ditch systems were not entirely covered by the study area because they were partly overbuilt. The circular ditch systems are related to the nearby farm 'Vroenhove', of which the name and historic accounts point to a medieval origin and probably revealed 'motte-and-baily' structure. During the 11th and 12th century local lords resided in these types of elite-settlements.

2.2. Multi-receiver EMI sensor

In its simplest configuration, an EMI soil sensor consists of two coils separated by a fixed distance. A primary magnetic field (H_p) is created by the transmitting coil carrying a time-varying electric current at a set frequency. This field creates eddy currents in the soil below, which induce their own magnetic field (H_i). Both the induced secondary field and the primary field are recorded by the receiving coil at a fixed distance from the transmitter coil (McNeill, 1980). The in-phase and quadrature-phase data are used to record the ratio of the H_i to the H_p. From the quadrature data, the σ_a of the bulk soil can be obtained, as a depth weighted conductivity value of the affected soil volume. We used the DUALEM-21S instrument (DUALEM, Milton, Canada), which consists of one transmitter coil and four receiver coils located at spacings of 1, 1.1, 2 and 2.1 m. The 1 and 2 m transmitter–receiver pairs form a vertical dipole mode (HCP-1 and HCP-2), while the 1.1 and 2.1 m pairs form a perpendicular dipole mode (PRP-1 and PRP-2). Both transmitter–receiver spacing and orientation determine the depth and weighting response pattern of the signal. The cumulative response (expressed as % of the measured signal, relative to 1) from the soil volume above a depth z (in m) was given by McNeill (1980) for the vertical ($R_{HCP,s}(z)$) dipole mode and by Wait (1962) for the perpendicular ($R_{PRP,s}(z)$) dipole mode:

$$R_{HCP,s}(z) = 1 - \left(4 \cdot \frac{z^2}{s^2} + 1\right)^{-0.5} \quad (1)$$

$$R_{PRP,s}(z) = 2\frac{z^2}{s^2}\left(4\frac{z^2}{s^2} + 1\right)^{-0.5} \quad (2)$$

with s being the transmitter–receiver spacing in m.

The depth of exploration (DOE), taken as the depth where the cumulative response reaches 70%, differs from 0.5 m, 1.0 m, 1.5 m to 3.2 m for the PRP-1, PRP-2, HCP-1 and HCP-2 coil configurations, respectively (Saey et al., 2009a). Our EMI sensor was pulled in a non-metal sled by an all-terrain vehicle at a speed of about 5–8 km h^{-1}, crossing the field at parallel lines spaced 0.85 m. Within the lines, measurement intervals were at approximately 0.25 m.

2.3. GPR system

Investigation of the subsurface by GPR is based on the penetration and reflection of high-frequency electromagnetic waves in the ground (Tye et al., 2011). The v of the downward-propagating wave depends on relative dielectric permittivity ε_r according to:

$$\varepsilon_r = \left(\frac{c}{v}\right)^2 \quad (3)$$

with c the speed of light in a vacuum, 0.2998 m ns^{-1} and $\varepsilon_r = \frac{\varepsilon}{\varepsilon_0}$ where ε_0 is the permittivity of free space.

Therefore, propagation changes are generally dominated by relative permittivity contrasts between two different media, and these determine the amplitude of any reflections generated (Davis and Annan, 1989). The reflection strength depends on the abruptness and contrast in ε_r across the boundaries between the different media, as well as the distance separating the interfaces and the antenna frequency used. Travel time measurements from GPR reflections can be used to determine v to an interface. The travel time of the high-frequency electromagnetic wave through each distinct soil layer can be calculated as the difference in arrival times of the reflections from the interfaces. Generally, v at each point of the transect can be estimated by using the difference between the two-way travel

times of upper and lower boundary (Δt) of each layer and the known average thickness (d) of each layer:

$$v = \frac{2 \cdot d}{\Delta t} \tag{4}$$

The depth of the interface z between two layers with a different ε_r can be calculated as:

$$z = \frac{t}{2} \cdot v \tag{5}$$

Finally, v can be converted into the ε_r according to Eq. (3). Using a site-specific or general empirical relationship (i.e. Topp et al., 1980), the ε_r estimates can be converted to the volumetric water content as done by Lunt et al. (2005).

In this study, a pulseEKKO PRO GPR system (Sensors & Software, Mississauga, Canada) was used, with a 500 MHz antenna. The in-line sampling interval was 0.05 m, the line spacing was 0.25 m. Relatively standard processing was applied. Different processing steps were applied in the following sequence: (i) a dewow filter, (ii) the alignment of the first peaks following the start of the air-wave, (iii) a bandpass filter with cut-off frequencies of 100 MHz and 1 GHz, (iv) an algorithm for removing horizontal linear background noise, (v) a de-spiking algorithm, (vi) interpolation to a 0.05 m × 0.05 m grid using a bicubic interpolation algorithm, and (vii) three-dimensional phase-shift migration. The dewow process was used to remove slowly-decaying low-frequency signals that are induced due to the proximity of the transmitter, receiver and soil, because their signals tend to saturate sectors in the images of the data. The background subtraction was used to remove horizontal bands in the images by replacing each trace by the original trace minus the average trace, calculated along all the traces in the profile (Bonomo et al., 2012). The band-pass filtering was applied to remove frequency components outside the intervals of interest. The high-amplitude spikes probably originated from the electric fence around the study site, and were replaced by the mean of the two adjacent traces. The data were analyzed by representing them in standard vertical sections and constant-time slices with a thickness of 1 ns, revealing informative plan-view structures.

3. Results and discussion

3.1. ECa survey

Table 1 gives the summary statistics of the four data sets of each 44,184 σ_a measurements. The mean values increase with increasing DOE, indicating the deeper material to be more conductive than the topsoil. Contrarily, the standard deviations decrease with increasing DOE, which indicates a smaller variation at increased depths below the soil surface.

Ordinary kriging was used to interpolate the measurements to a 0.1 by 0.1 m grid. Hereby, a maximum of 64 neighbors was used within a circular search area around the location being interpolated. Fig. 2 shows the resulting σ_a maps of the study area with a common legend scale for comparative reasons. The overall pattern of the four σ_a maps is similar, i.e. a broad circular structure (A on Fig. 2b) surrounded by a narrow, square structure (B on Fig. 2b) and high values near the south-eastern border of the study site.

Table 1
Descriptive statistics (m: mean, min: minimum, max: maximum, s: standard deviation) of $\sigma_{a,PRP,1}$, $\sigma_{a,PRP,2}$, $\sigma_{a,HCP,1}$ and $\sigma_{a,HCP,2}$ for the study site (44,184 measurement points).

Variable	m (mS m^{-1})	min (mS m^{-1})	max (mS m^{-1})	s (mS m^{-1})
$\sigma_{a,PRP,1}$	4	−81	92	4
$\sigma_{a,PRP,2}$	6	−76	55	4
$\sigma_{a,HCP,1}$	8	−107	83	4
$\sigma_{a,HCP,2}$	10	−15	83	3

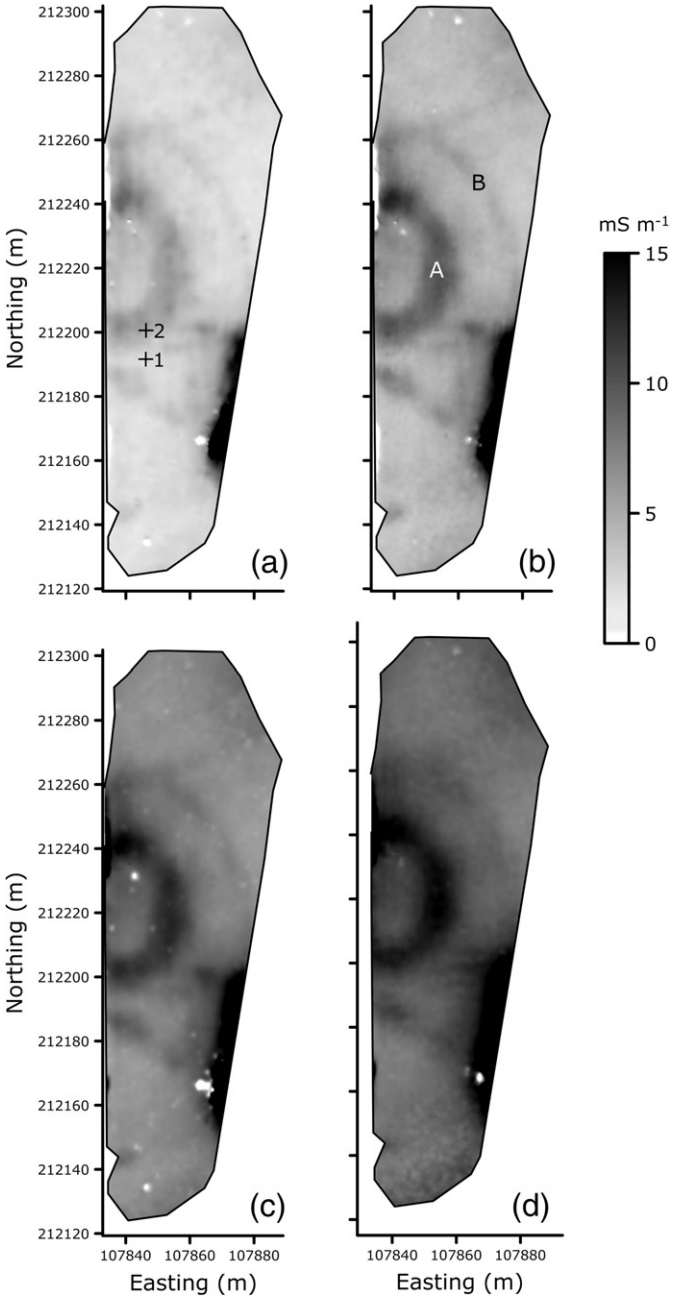

Fig. 2. σ_a measurements of the coil configurations PRP-1 with auger locations 1 and 2 (a), PRP-2 (b), HCP-1 (c) and HCP-2 (d).

3.2. Soil analyses

To evaluate both the soil profiles in and outside the main ditch, two auger locations were lcoated based on the σ_a: one outside the ditch (location 1 on Fig. 2a) and a second in the middle of the ditch (location 2 on Fig. 2a). At both locations, samples were taken up to a depth of 1.8 m at 0.2 m intervals. The samples were analyzed for their textural composition according to the conventional sieve–pipette method and for their organic matter content (SOM) according to the Walkley and Black method. The textural fraction with boundaries 0–50 μm (clay and silt) and SOM were determined and

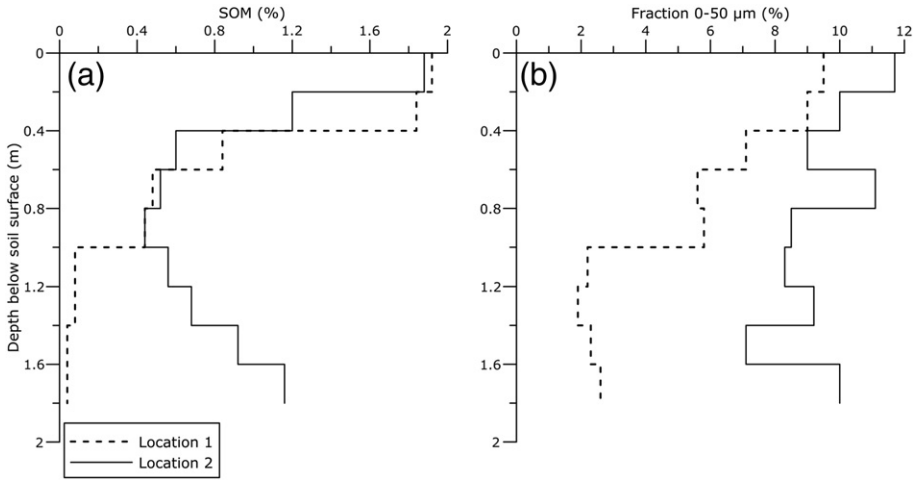

Fig. 3. Analyzed organic matter content (SOM) (a) and content of fraction 0–50 µm (b) at locations 1 and 2 up to a depth of 1.8 m.

shown in Fig. 3. From this it could be deduced that the ditch system contains both a higher content of fine material (textural fraction 0–50 µm) across the entire soil profile and a higher SOM content from 1.0 m depth. At a depth of 1.8 m, the SOM of the ditch and the surrounding soil differs by more than 1%. These differences indicate an infilling of the ditch with finer, organic rich material.

3.3. GPR survey

Both circular ditches are detected as low-amplitude anomalies on both the GPR time slices (Fig. 4) and profiles (Fig. 5b), because these ditches are characterized by the absence of reflections compared to the surrounding soil. These concentric ditches (one larger

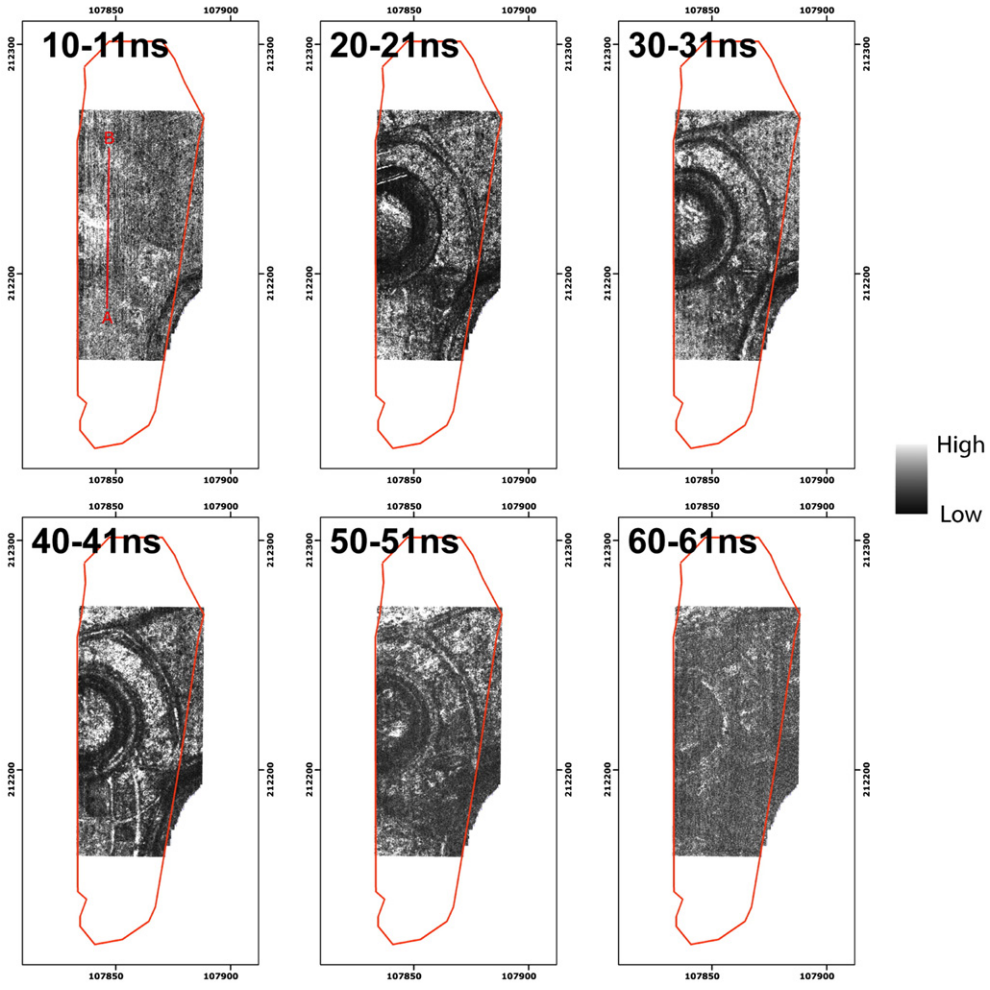

Fig. 4. GPR time-slices of the study site (at given time intervals) and location of transect AB.

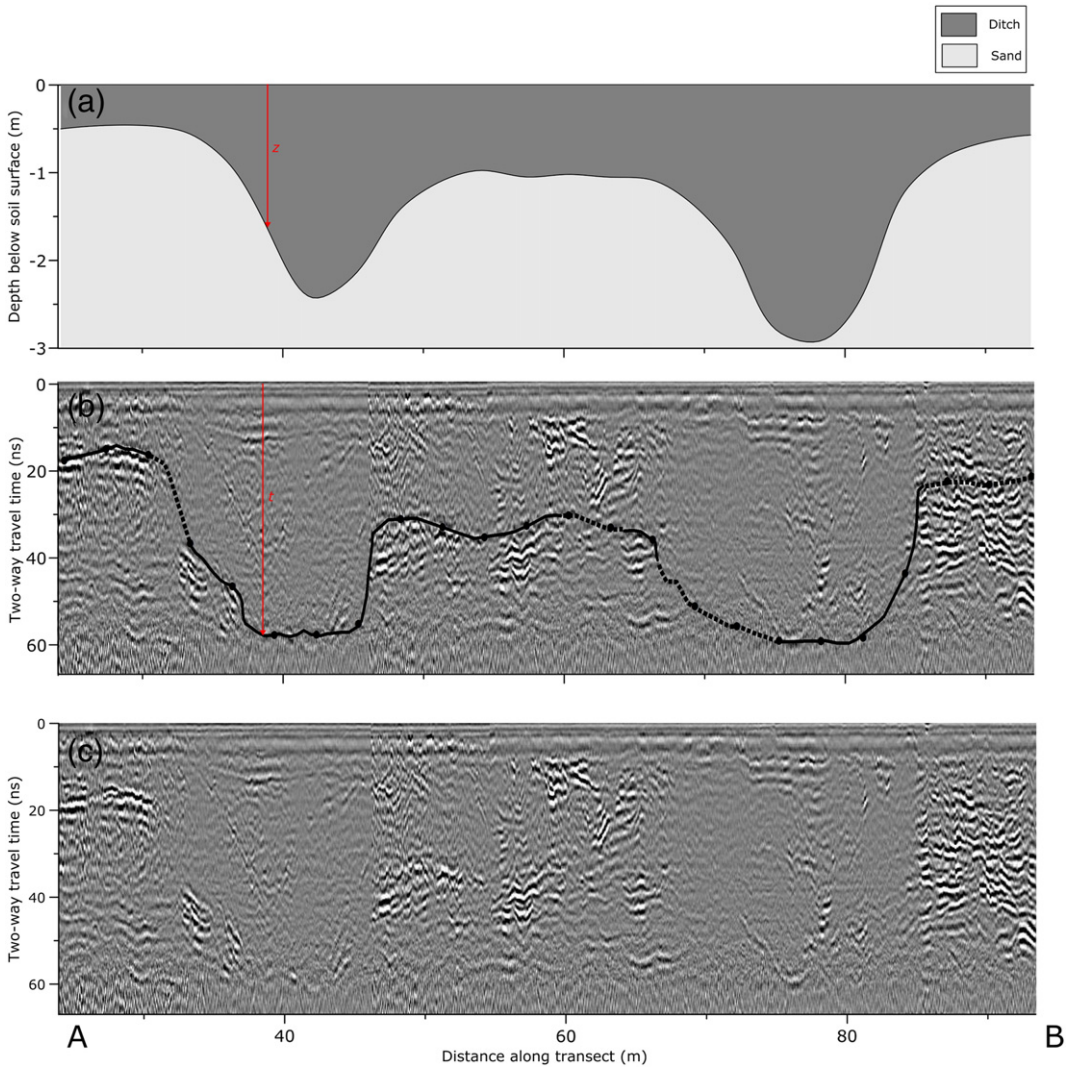

Fig. 5. Modeled depth of the ditch system z^* (a), GPR profile with 24 digitized two-way travel times t of the ditch-sand interface and interpolated line (b) and GPR profile (c) along transect AB.

circular ditch and one smaller square ditch) come across on the time slices between a t of 10 ns and 62 ns, as shown in Fig. 4. For every ditch, within the negative anomalies also high-amplitude anomalies (zones with strong reflection) are present. These are probably due to the way the ditches were filled: one phase where homogeneous material was slowly deposited along the ditch walls, and a second, probably shorter phase where more heterogeneous material was deposited in the remaining central part of the ditches.

The PulseEKKO GPR profiles show clear reflections where the sandy material is present. Therefore, we assumed a simplified two-layered soil model with a distinct interface between the ditch infilling and the sandy material, although the real stratigraphy can be more complicated. On the GPR profiles, the boundary between both layers was digitized and gathered as t at each of the 24 locations along transect AB (Fig. 5b). At some parts of the transect however (between 32 and 35 m, between 61 and 65 m, between 68 and 76 m and beyond 87 m, visualized as dashed lines in Fig. 5b), the interface does not show clearly within the GPR profile. Nevertheless, we connected the sharpest continuous reflections bordering these less clearly defined boundaries. It should also be noted that the bottom boundary of the ditches is sometimes difficult to acknowledge, because it is situated nearby the depth where the GPR signal starts to attenuate.

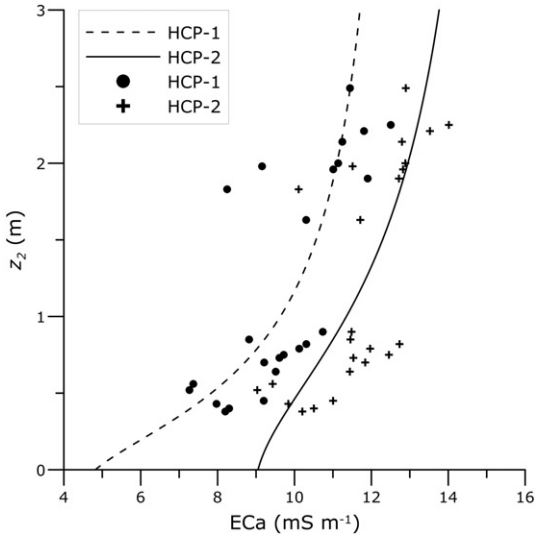

Fig. 6. Fitted cumulative depth response curves (and expressed as depth (z) apparent electrical conductivity (σ_a) relationship) (a) for both HCP-s coil configurations with their corresponding z–σ_a observations.

3.4. Depth modeling

A transect AB was laid out in such a way that the wide circular ditch, visible on the EMI measurements, was visited twice (Fig. 4). To model the morphology of the ditch system, we assumed a two-layered soil system with a ditch infilling situated above a sandy subsoil layer. The objective was to model the depth to the interface z between these two layers. Because the ditch system extends beyond a depth of 1.5 m, both σ_a measurements (1 and 2 m HCP) with the highest DOE were used for modeling z. The integration of these deeper ECa measurements should be able to capture small differences in depth of the ditch-sand interface.

We developed an inversion procedure which allowed to model simultaneously the conductivity values of the ditch infilling layer (σ_{ditch}), the subsoil sandy layer (σ_{sand}) and the propagation speed v. This was done by equating the modeled σ_a from the HCP-2 coil configuration ($\sigma^*_{a,HCP,2}$) to the measured $\sigma_{a,HCP,2}$ and employing the t deduced from

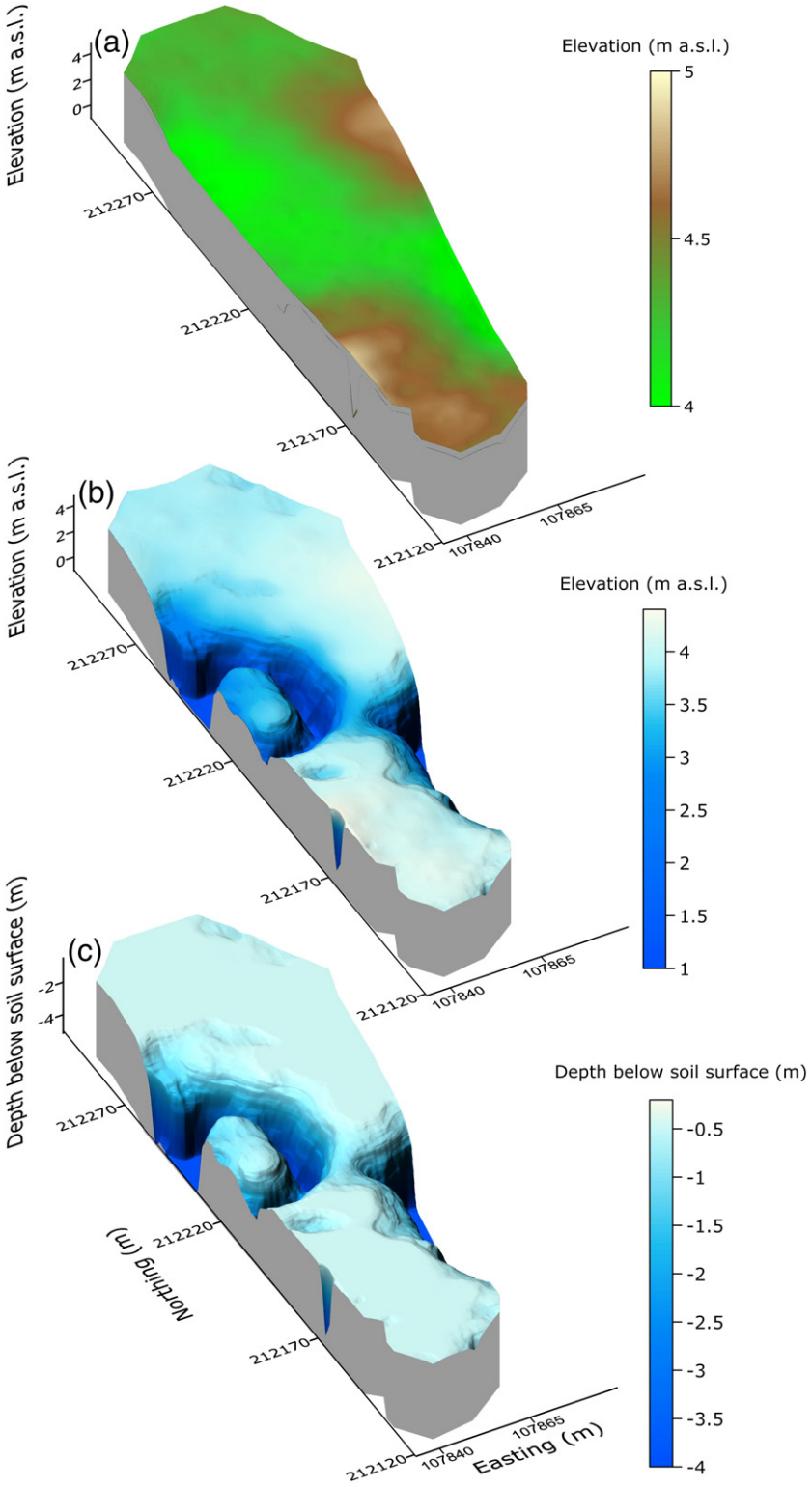

Fig. 7. Elevation of the current soil surface of the study area Z (a) and of the modeled bottom of the ditch Z–z^* (b); (c) shows the depth of the ditch-sand interface below the soil surface (z^*).

the GPR profile at 24 locations along transect AB. In a two-layered soil build-up, multiplying the relative weight with the σ of each layer and adding up all the layers results in the total $\sigma^*_{a,HCP,s}$ of the investigated medium:

$$\sigma^*_{a,HCP,s} = \left[R_{HCP,s}\left(v^* \cdot \frac{t}{2}\right) - R_{HCP,s}(z_s)\right] \cdot \sigma^*_{ditch,HCP,s} + \left[1 - R_{HCP,s}\left(v^* \cdot \frac{t}{2}\right)\right] \cdot \sigma^*_{sand,HCP,s} \quad (6)$$

with z_s the height of the sensor above the soil (0.16 m). $R_{HCP,s}(z)$ is given by Eq. (1). To obtain the model parameters $\sigma^*_{ditch,HCP,2}$, $\sigma^*_{sand,HCP,2}$ and v^*, the sum of the squared differences between $\sigma^*_{a,HCP,2}$ and $\sigma_{a,HCP,2}$ was minimized for the 24 measurement locations across transect AB:

$$\sum_{i=1}^{n}\left[\sigma^*_{a,HCP,2}(i) - \sigma_{a,HCP,2}(i)\right]^2 = \min \quad (7)$$

with i the number of the measurement along transect AB and n the total amount of measurements (24). The parameters $\sigma^*_{ditch,HCP,2}$, $\sigma^*_{sand,HCP,2}$ and v^* were found to be respectively 17 mS m^{-1} and 9 mS m^{-1} and 0.0728 m ns^{-1}. The same procedure was applied to the HCP-1 coil configuration, given the found propagation speed v^*. Again the conductivity values were modeled by minimizing the difference between the modeled $\sigma^*_{a,HCP,1}$ and the observed $\sigma_{a,HCP,1}$. This resulted in conductivity values of 14 mS m^{-1} and 5 mS m^{-1} for both $\sigma^*_{ditch,HCP,1}$ and $\sigma^*_{sand,HCP,1}$. Fig. 6 shows the cumulative response curves (expressed as z–σ_a relationship (Eqs. (1) and (6)) given the modeled conductivities $\sigma^*_{ditch,HCP,s}$ and $\sigma^*_{sand,HCP,s}$ for both coil configurations) plotted against their 24 corresponding z–σ_a observations. The modeled response curves coincide well with the observation points. Although the coefficients of determination (R^2) are high (0.81 and 0.76 for the HCP-1 and HCP-2 coil configurations), the modeled relationship overestimates the real z at low σ_a.

At each of the 44,184 DUALEM-21S measurement locations, both $\sigma_{a,HCP,1}$ and $\sigma_{a,HCP,2}$ were simultaneously inverted by solving the set of two Eq. (6) to model z^*, given the obtained parameters ($\sigma^*_{ditch,HCP,s}$ and $\sigma^*_{sand,HCP,s}$) for each coil configuration (Marquardt, 1963).

3.5. Reconstruction of the ditch-sand interface

The elevation of the soil surface (Z), obtained from the DGPS measurements, and z^* were interpolated and the result is given in Fig. 7a and c. z^* was subtracted from Z and the resulting terrain model is shown in Fig. 7b, representing the elevation of the ditch-sand interface. Fig. 7b and c represents the main ditch and its dimensions. Along 70 m transect AB (Fig. 5a) the infilling has a modeled width of 20 m and a depth of maximally 2.9 m, with the northern part of the ditch extending deeper into the sandy subsoil.

3.6. Verification

Along the 70 m transect AB, 24 observation points were located at 3 m intervals. At 21 points, z was observed visually by augering. This ditch infilling was clearly distinguishable from the underlying sand, because of the substantially higher SOM content, darkening the soil within the ditch. At the remaining five locations, no ditch infilling was present. In those cases, z was observed as the depth between the organic rich topsoil and the underlying coarse sand. On average, the observed z was 1.42 ± 0.64 m, with a minimum of 0.43 m outside the ditch and a maximum of 2.49 m in the center of the ditch.

First, the observed z was compared with the modeled z^* after inverting both HCP σ_a measurements simultaneously. The sum of the squared differences between z and z^* was minimized at the 24 locations along transect AB. This model evaluation resulted in a correlation coefficient of 0.94, a MEE of 0.02 m and a RMSEE of 0.25 m, which confirms the accurateness of the model in predicting the morphology of the ditch system (Fig. 8). However, the model tends to overestimate the greater depths.

The modeled propagation speed was verified by fitting z^*, calculated from the t up to the ditch-sand interface, to the observed z. This allowed to estimate the propagation speed of the GPR signal up to the interface. The resulting v appears to be 0.0712 m ns^{-1}, which is only slightly different from the before obtained v^* of 0.0728 m ns^{-1}. With a v of 0.0712 m ns^{-1}, the MEE, RMSEE and correlation between z and z^* are respectively 0.03 m, 0.16 m and 0.97, which means that there is a small bias, a high accuracy and a high correlation. Therefore, it can be concluded that the propagation speed of 0.0728 m ns^{-1} is a realistic approximation of the propagation speed up to the ditch-sand interface. Moreover, constant-velocity migration tests (CVMT) using a 2-D frequency-wavenumber migration algorithm were conducted with velocities ranging from 0.05 to 0.15 m/ns. For the diffraction hyperbolas at different two-way travel times, the velocity that best collapsed the hyperbolas was recorded. The resulting average velocity was exactly the same as v^* (0.0728 m ns^{-1}). Therefore, the CVMT estimate has proven appropriate to determine the propagation velocity in situations where no invasive practices through coring are allowed.

Furthermore, Eq. (3) was used to transform the obtained v^* into ε_r. For the ditch infilling, a ε_r of 17 was obtained, corresponding with the values proposed by Conyers (2004) for organic-rich agricultural land and by Jol (2009) for a wet, sandy soil.

3.7. Integrated visualization

The propagation speed of 0.0728 m ns^{-1} up to the variable t, allows to attribute real depths to the GPR time slices. Therefore, a slice at t coincides with a depth of:

$$z = \frac{t}{2} \cdot 0.0728\text{m ns}^{-1} \quad (9)$$

This modeled propagation velocity corresponds to the propagation speed within the ditch infilling. Therefore, attributing depths to these slices is only realistic at places where the ditch infilling is present. The wave velocity within the sandy subsoil could not be determined due to the absence of a clear reflector at the bottom of this homogeneous subsoil.

As an example, the 26 to 27 ns and 47 to 48 ns time slices were plotted jointly with the three-dimensional ditch-sand interface, obtained after inverting the σ_a measurements (Fig. 9). These time slices correspond with the modeled depths of 0.96 m (Fig. 9a) and 1.73 m

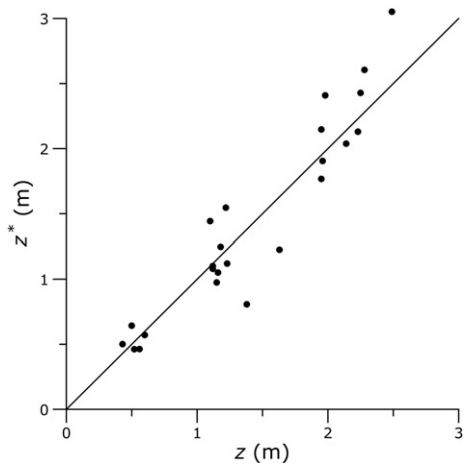

Fig. 8. The modeled depths (z^*) plotted versus the observed depths (z) at the 24 locations along transect AB.

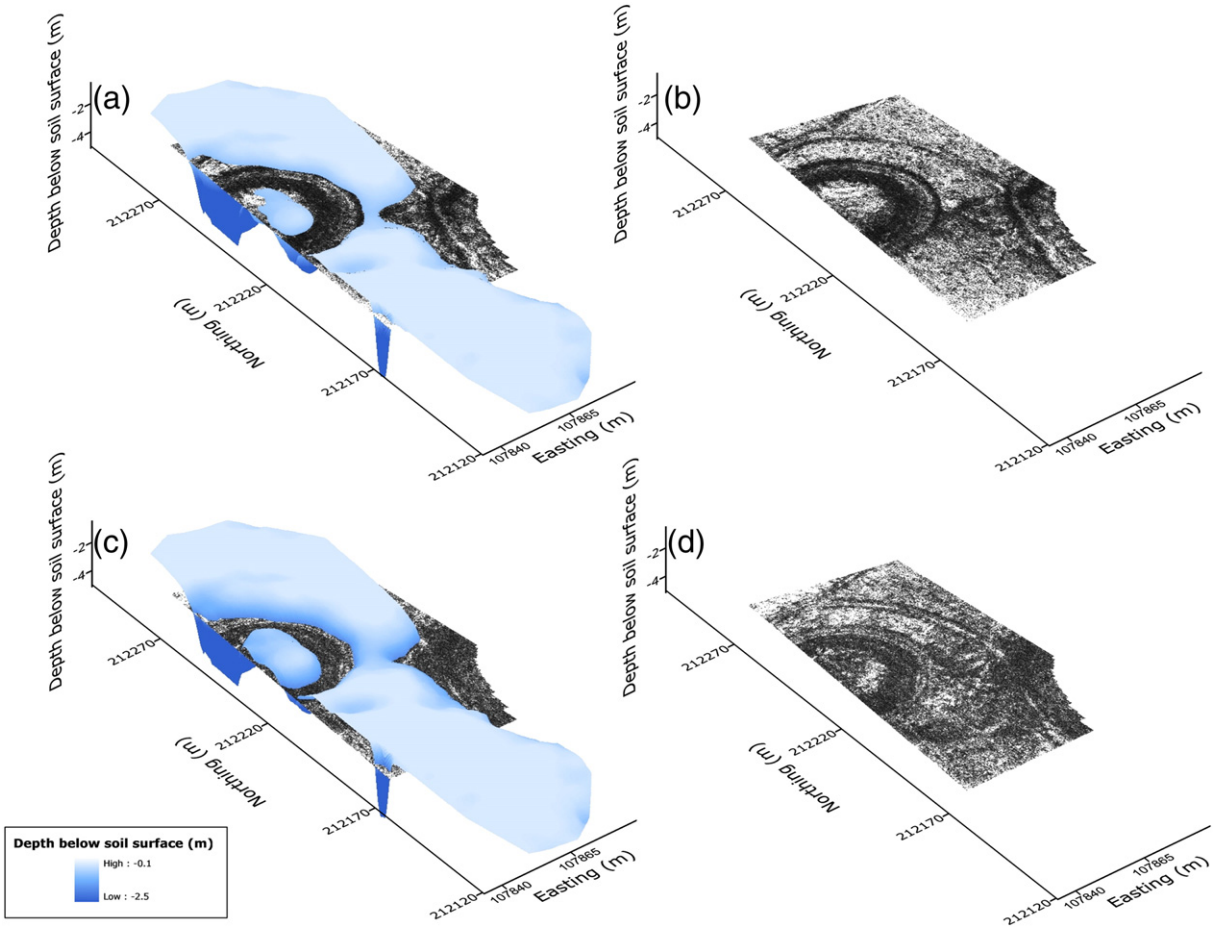

Fig. 9. Three-dimensional representation of the depth of the ditch-sand interface (z^*) with GPR depth slice between 26 and 27 ns, which coincides with a modeled depth of 0.96 m (a), GPR depth slice between 24 and 27 ns (b), z^* with GPR depth slice between 47 and 48 ns, which coincides with a modeled depth of 1.73 m (c), GPR depth slice between 47 and 48 ns (d).

(Fig. 9c) respectively. This integrated visualization strongly improves the interpretation of the three-dimensional context. Moreover, it can be merged with the cross-sectional representation of GPR depth slices. This provides a greatly improved clarity of view, constituting a valuable perceptive and didactic tool for the integrated visualization of soil geophysical data.

4. Conclusions

A methodology to integrate complementary geophysical techniques was proposed. The integrated EMI depth modeling and GPR depth slicing procedures allowed to model the exact depth of the interface between the ditch infilling and the underlying soil (with a MEE of 0.02 m and a RMSEE of 0.25 m). The developed methodology enabled the simultaneous quantification of the EMI inversion parameters and the propagation speed of the high-frequency GPR waves in the soil. It can be of use when no invasive practices are allowed and when the same feature appears on both GPR and EMI measurements. This method can be considered an alternative to the conventional methods employed to determine the dielectric permittivity and the conductivities of both layers in a two-layered soil model, but the integration of both complementary, non-invasive techniques has never been performed before.

To conclude, the integrated approach yielded a detailed and non-invasive vertical characterization of subsoil features. Moreover, co-visualizing of both the three-dimensional ditch interface, derived from inverting the multi-receiver EMI signals, and the GPR depth slices can be employed as a tool to aid the interpretation of archeological and soil-geomorphological data.

Acknowledgments

The authors would like to thank Valentijn Van Parys for his assistance with the field work and the farmer Ronny Perneel for granting us access to his field.

References

Beamish, D., 2011. Low induction number, ground conductivity meters: a correction procedure in the absence of magnetic effects. J. Appl. Geophys. 75, 244–253.
Bonomo, N., Osella, A., Martinelli, P., de la Vega, M., Cocco, G., Letieri, F., Frittegotto, G., 2012. Location and characterization of the Sancti Spiritus Fort from geophysical investigations. J. Appl. Geophys. 83, 57–64.
Conyers, L.B., 2004. Ground-Penetrating Radar for Archaeology. Altamira Press, Rowman & Littlefield Publishers Inc., Walnut Creek, California, USA.
Davis, J.L., Annan, A.P., 1989. Ground-penetrating radar for high-resolution mapping of soil and rock stratigraphy. Geophys. Prospect. 37, 531–551.
Huisman, A., Hubbard, S.S., Redman, J.D., Annan, A.P., 2003. Measuring soil water content with ground penetrating radar: a review. Vadose Zone J. 2, 476–491.
Jol, H.M., 2009. Ground-Penetrating Radar: Theory and Applications. Elsevier Science, Amsterdam, The Netherlands.
Kvamme, K., 2006. Integrating Multidimensional Geophysical Data. Archaeol. Prospect. 13, 57–72.
Lunt, I.A., Hubbard, S.S., Rubin, Y., 2005. Soil moisture content estimation using ground-penetrating radar reflection data. J. Hydrol. 307, 256–269.
Marquardt, D., 1963. An algorithm for least-squares estimation of nonlinear parameters. SIAM J. Appl. Math. 11, 431–441.
McNeill, J.D., 1980. Electromagnetic terrain conductivity measurement at low induction numbers. Technical Note TN-6. Geonics Limited, Missisauga, Ontario, Canada.

Reynolds, J.M., 1997. An Introduction to Applied and Environmental Geophysics. John Wiley & Sons Ltd., Chichester, England.
Saey, T., Simpson, D., Vermeersch, H., Cockx, L., Van Meirvenne, M., 2009a. Comparing the EM38DD and DUALEM-21S Sensors for Depth-to-Clay Mapping. Soil Sci. Soc. Am. J. 73, 7–12.
Saey, T., Van Meirvenne, M., Vermeersch, H., Ameloot, N., Cockx, L., 2009b. A pedotransfer function to evaluate the soil profile textural heterogeneity using proximally sensed apparent electrical conductivity. Geoderma 150, 389–395.
Saey, T., Islam, M.M., De Smedt, P., Meerschman, E., Meeuws, F., Van De Vijver, E., Lehouck, A., Van Meirvenne, M., 2012. Using a multi-receiver survey of apparent electrical conductivity to reconstruct a Holocene tidal channel in a polder area. Catena 95, 104–111.
Sucre, E.B., Tuttle, J.W., Fox, T.R., 2011. The use of ground-penetrating radar to accurately estimate soil depth in rocky forest soils. For. Sci. 57, 59–66.
Sys, C., Vandenhoudt, H., 1974. Bodemkaart van Belgie, Verklarende tekst bij het kaartblad Bassevelde 25 W. Centrum voor Bodemkartering (Dir. R Tavernier), Gent.
Topp, G.C., Davis, J.L., Annan, A.P., 1980. Electromagnetic determination of soil water content: measurements in coaxial transmission lines. Water Resour. Res. 16, 574–582.
Tye, A.M., Kessler, H., Ambrose, K., Williams, J.D.O., Tragheim, D., Scheib, A., Raines, M., Kuras, O., 2011. Using integrated near-surface geophysical surveys to aid mapping and interpretation of geology in an alluvial landscape within a 3D soil-geology framework. Near Surf. Geophys. 9, 15–31.
Wait, J.R., 1962. A note on the electromagnetic response of a stratified earth. Geophysics 27, 382–385.